

On the relative performance of edge illumination x-ray phase contrast CT and conventional, attenuation-based CT

Charlotte Klara Hagen,^{1, a)} Paul Claude Diemoz,¹ and Alessandro Olivo¹

Department of Medical Physics and Bioengineering, University College London, Malet Place, Gower Street, London WC1E 6BT, UK

Purpose: This article is aimed at comparing edge illumination (EI) x-ray phase contrast computed tomography (PCT) and conventional (attenuation-based) computed tomography (CT), based on their respective contrast and noise transfer.

Methods: The noise in raw projections obtained with EI PCT is propagated through every step of the data processing, including phase retrieval and tomographic reconstruction, leading to a description of the noise in the reconstructed phase tomograms. This is compared to the noise in corresponding attenuation tomograms obtained with CT. Specifically, a formula is derived that allows evaluating the relative performance of both modalities on the basis of their contrast-to-noise ratio (CNR), for a variety of experimental parameters.

Results: The noise power spectra of phase tomograms are shifted towards lower spatial frequencies, leading to a fundamentally different noise texture. The relative performance of EI PCT and CT, in terms of their CNR, is linked to spatial resolution: the CNR in phase tomograms is generally superior to that in attenuation tomograms for higher spatial resolutions (tens to hundreds of μm), but inferior for lower spatial resolutions (hundreds of μm to mm).

Conclusions: These results imply that EI PCT could outperform CT in applications for which high spatial resolutions are key, i.e. small animal or specimen imaging.

Keywords: Phase contrast imaging, Computed tomography, X-ray imaging

I. INTRODUCTION

Conventional x-ray computed tomography ('CT' in the following) and x-ray phase contrast computed tomography ('PCT' in the following) are two imaging modalities that provide cross-sectional images ('tomograms'). These are reconstructed from projections of a sample, which is rotated over a range of at least 180 degrees. In CT, contrast is due to x-ray attenuation caused by photoelectric absorption or Compton scatter. In PCT, contrast arises from phase shifts caused by variations of the wave velocity in different media. Attenuation (A) and phase shifts (Φ) are commonly expressed as:

$$A_{\theta}(x, y; k) = 2k \int_{-\infty}^{\infty} \beta(x', y', z'; k) dz \quad (1)$$

$$\Phi_{\theta}(x, y; k) = k \int_{-\infty}^{\infty} \delta(x', y', z'; k) dz, \quad (2)$$

where z is the beam propagation direction, (x, y) describes the measurement plane, $(x', y', z') = (x \cdot \cos(\theta) + z \cdot \sin(\theta), y, -x \cdot \sin(\theta) + z \cdot \cos(\theta))$ are the coordinates of the rotating sample, θ is the rotation angle, k is the wave number, and δ and β are the real and imaginary components of the complex refractive index ($n = 1 - \delta + i\beta$). Tomograms produced by CT and PCT show maps of the quantities β ('attenuation tomograms') and δ ('phase tomograms'), respectively.

CT can be implemented with a relatively simple experimental setup and a moderate amount of data processing. In essence, a detector is placed downstream of

the sample, where it measures the transmitted intensity (I_{tr}). Raw projections can be described by Beer's law: $I_{tr, \theta}(x; k) = N_0 \cdot \exp(-A_{\theta}(x; k))$, where N_0 is the number of photons incident on the sample. Here, a transverse cross-section was considered (i.e. y constant). Attenuation images can then be recovered via: $A_{\theta}(x; k) = -\log(I_{tr, \theta}(x; k)/N_0)$, from which tomograms can be reconstructed, provided θ covers the necessary 180 degree range. PCT typically requires a more sophisticated approach, as phase shifts must be converted into detectable intensity variations. Several methods to do this exist¹. Propagation-based imaging²⁻⁴ exploits the fact that phase shifted and non-phase shifted beam portions interfere and give rise to measurable intensity fringes, provided a sufficient degree of spatial coherence is present. Talbot/Lau interferometry⁵⁻⁷ is based on the Talbot effect, which creates an interference pattern in the form of a self-image at specific distances downstream of a diffraction grating. Phase shifts by the sample disturb this pattern, which can be detected. Analyzer-based imaging⁸⁻¹⁰ exploits the fact that phase shifts locally change the direction of the beam (refraction) which, by introducing a crystal in the beam path, is translated into an increased/decreased intensity reaching the detector. A similar concept is used by aperture-based methods (e.g. edge illumination^{11,12}), which employ a single aperture/an array of apertures to convert directional beam changes into measurable intensity variations. All PCT methods have in common the fact that phase shifts are encoded in the raw projections, and that dedicated data processing ('phase retrieval') must be applied prior to tomographic reconstruction.

Naturally, the coexistence of CT and PCT raises the question of their relative performance. On the one hand,

^{a)} charlotte.hagen.10@ucl.ac.uk

This article has been accepted for publication and undergone full peer review but has not been through the copyediting, typesetting, pagination and proofreading process, which may lead to differences between this version and the Version of Record. Please cite this article as doi:

10.1002/mp.12179

This article is protected by copyright. All rights reserved.

for many weakly attenuating specimens and within the diagnostic energy range of x-rays, differences in δ ($\sim 10^{-7} - 10^{-6}$) can be up to three orders of magnitude larger than differences in β ($\sim 10^{-10} - 10^{-9}$), implying that phase tomograms feature a higher intrinsic contrast than attenuation ones. On the other hand, image quality is ultimately determined not by contrast, but by the contrast-to-noise ratio (CNR), making it necessary to analyze the noise transfer in both modalities in order to compare them. Detailed noise analyses have been performed for most PCT methods^{13–19}; however, no noise analysis has so far been performed for edge illumination (EI) PCT. With this article, we aim to fill this gap. Our analysis follows the approach by Raupach and Flohr¹⁵, as their formalism can be applied to any differential PCT method, including Talbot/Lau interferometry, analyzer-based imaging and aperture-based methods.

This article is organized as follows. After briefly reviewing EI PCT in terms of the image formation, phase retrieval and tomographic reconstruction (Section II), we analyze theoretically how noise in the raw projections is propagated into the reconstructed phase tomograms (Section III). Finally, we exploit our theory to evaluate the noise performance of EI PCT relative to that of CT (Section IV). Specifically, we derive formulas that enable a direct comparison of the two modalities on the basis of their CNR. The article concludes with a summary and a discussion of the results (Section V), including the limitations of the presented analysis.

II. EDGE ILLUMINATION PCT

A. Image formation

The working principle of EI PCT is schematically shown in Fig. 1: a mask in front of the sample ('pre-sample mask') splits the incoming x-ray beam into an array of individual beamlets, with a lateral inter-beamlet distance sufficient to keep them physically separated. A second mask ('detector mask'), positioned in front of the detector, creates insensitive regions between adjacent pixel rows/columns. When the first mask is slightly offset with respect to the second one, such that each beamlet falls on the edge of one of the apertures of the detector mask, directional beam changes caused by refraction are translated into an increased or decreased detected intensity. Thus, raw projections contain both attenuation and refraction information, which, assuming that small angle scattering can be neglected, can be described by^{21,22}:

$$I_{L,\theta}(Mx; k) = N_0 \cdot e^{-A_\theta(x; k)} \cdot C \left(x_L + \frac{z_2 \alpha_\theta(x; k)}{M} \right), \quad (3)$$

where M is the geometric magnification ($M = (z_1 + z_2)/z_1$), z_1 and z_2 are the source-to-sample mask and sample mask-to-detector distances, respectively, and $\alpha_\theta(x; k)$ is the refraction angle, which is related to the

phase shift via: $\alpha_\theta(x; k) = (1/k) \cdot \partial\Phi_\theta(x; k)/\partial x$. The symbol C denotes the illumination function, which is measured before any EI PCT scan (in the absence of the sample) by step-scanning the pre-sample mask along the x-direction. For imaging, the pre-sample mask is then kept in a fixed position x_L (the so-called 'working point'), which typically corresponds to the steepest point on either of its slopes. In Eq. 3, x_L was assumed to be on the left (ascending) slope. An exemplary illumination function, corresponding to the parameters listed in Table I (Section IV A), is shown in Fig. 2(a).

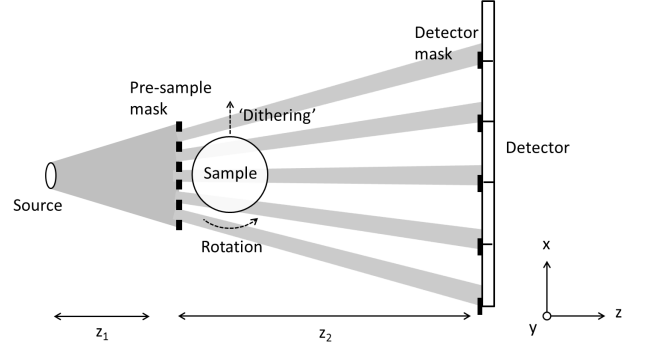


FIG. 1. Schematic of an EI PCT setup (not to scale).

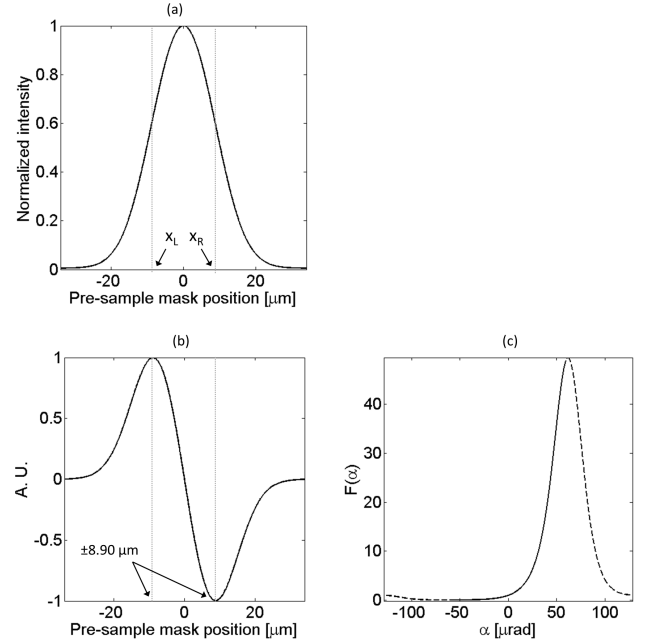


FIG. 2. (a) Illumination function C simulated for parameters listed in Table I (Section IV A) with indicated left and right slope working points (x_L , x_R), (b) the first derivative of the illumination function with indicated maxima and minima, which correspond to x_L and x_R , (c) the function F , which relates the refraction angle to the ratio of two raw EI PCT projections. The injective part is indicated by the non-dashed part of the line

Note that, while in Eq. 3 the x-coordinate was assumed to be a continuous variable, in practice projections are sampled at discrete locations $x_i = x_0 + id$, with d being the sampling step. If no additional sample movement is applied except rotation, d is equal to the pre-sample mask period. However, this can be artificially increased through ‘dithering’, i.e. displacing the sample multiple times for each projection by a fraction of the pre-sample mask period, acquiring data for each displacement, and combining them into a single dataset featuring a higher sampling rate²³. In that case, d is equal to the sample displacement. Dithering can be performed in a discrete (the sample is kept stationary while the detector is acquiring, and is displaced during read-out) or continuous manner (the sample is moved continuously throughout the acquisition)²⁴. In the following, it is assumed that EI PCT data are acquired with continuous dithering.

B. Phase retrieval and tomographic reconstruction

The refraction contribution to Eq. 3 must be extracted as a prerequisite for the reconstruction of phase tomograms. Previous work^{21,22} has demonstrated that this can be achieved if, at each rotation angle, two raw projections ($I_{L,\theta}$, $I_{R,\theta}$) are acquired with working points on the left and right slopes of the illumination function. The refraction angle image (α_θ), can then be obtained according to:

$$\alpha_\theta(x_i; k) \approx F^{-1} \left(\frac{I_{L,\theta}(Mx_i; k)}{I_{R,\theta}(Mx_i; k)} \right), \quad (4)$$

where F is a function that, apart from α_θ , depends only on known parameters:

$$F(\alpha_\theta) = \frac{C \left(x_L + \frac{z_2 \alpha_\theta}{M} \right)}{C \left(x_R + \frac{z_2 \alpha_\theta}{M} \right)}. \quad (5)$$

Before its inversion, F has to be restricted to its injective part, which defines the range of retrievable refraction angles. Figure 2(c) shows this function for the parameters listed in Table I (Section IV A).

Following the extraction of α_θ , the phase shift image (Φ_θ) can be recovered via a one-dimensional discrete integration:

$$\Phi_\theta(x_i; k) = k \cdot \Delta x \sum_{i'=0}^i \alpha_\theta(x_{i'}; k), \quad (6)$$

where the multiplicative weight is given by the sampling step ($\Delta x = d$). The application of tomographic reconstruction methods to Φ_θ (acquired over at least 180 degrees) then provides phase tomograms²⁵. Note that the explicit integration of α_θ to recover Φ_θ is not strictly necessary, as phase tomograms can also be reconstructed from α_θ directly if the integration step (Eq. 6) is incorporated into the reconstruction process. This can be

done, for example, by using the filtered back projection (FBP) algorithm in combination with the Hilbert filter²⁶. However, in order to be consistent with the analysis by Raupach and Flohr¹⁵, in the following the recovery of Φ_θ is treated as a separate step, which is mathematically equivalent to the Hilbert filter approach.

III. NOISE PROPAGATION

A. Methodology and assumptions

In order to analyze the noise performance of EI PCT, it is important to understand how noise in the raw projections ($I_{L,\theta}$, $I_{R,\theta}$) is propagated by the various steps of the data processing, which include the extraction of the refraction angle image (Eq. 4), recovery of the phase shift image (Eq. 6), and eventually tomographic reconstruction. In the following, this is separately discussed for each step. The noise is generally described by its variance (σ^2) and noise power spectrum (NPS). Further, the following assumptions are made:

- The noise in raw projections can be described according to an uncorrelated Poisson model, i.e. the variance is given by the mean number of detected photons, and the NPS is constant across all spatial frequencies.
- Phase and attenuation tomograms are acquired with the same number of photons (N_0) incident on the sample (i.e. with the same dose). The number of photons downstream of the sample is thus: $N = N_0 \cdot \exp(-A_\theta(x_i; k))$. Since in EI PCT two raw projections ($I_{L,\theta}$, $I_{R,\theta}$) are acquired at each angle, half of the total number of photons must be used for each of them, therefore:

$$I_{L,\theta}(x_i; k) = \frac{N}{2} \cdot C \left(x_L + \frac{z_2 \alpha_\theta(x_i; k)}{M} \right) \quad (7)$$

$$I_{R,\theta}(x_i; k) = \frac{N}{2} \cdot C \left(x_R + \frac{z_2 \alpha_\theta(x_i; k)}{M} \right). \quad (8)$$

- Phase and attenuation tomograms are acquired with the same detection efficiency. This allows neglecting factors relating to the detection efficiency in the subsequent formulas.
- Phase and attenuation tomograms are reconstructed with FBP with the Shepp-Logan filter.
- The spatial resolution in EI PCT and CT raw projections is the same, i.e. the setups have the same point spread function (PSF). In EI PCT, the PSF can be expressed as a multiplication of the source distribution (projected onto the sample plane) with a box function representing the pre-sample mask

aperture, which is then convolved with an additional box function representing the sample movement by distance d (sampling step) employed during the continuous dithering^{24,27}. Notably, it is independent from the pixel size, provided the pixel response is approximately constant over the width of the detector mask aperture. Thus, if d is large compared to the pre-sample mask aperture and the projected source, the PSF in EI PCT is approximately square with width d . In CT, this can be matched with a point source and pixels of size d with a perfectly square response.

To demonstrate that the spatial resolution in EI PCT and CT is indeed the same under the above assumptions, images of a $500 \mu\text{m}$ diameter wire were simulated for the respective modalities. For EI PCT, the parameters listed in Table I and a sampling step of $d = 68 \mu\text{m}$ were assumed. For CT, a matching pixel size and perfectly square response were assumed. The images and profile plots are shown in Fig. 3.

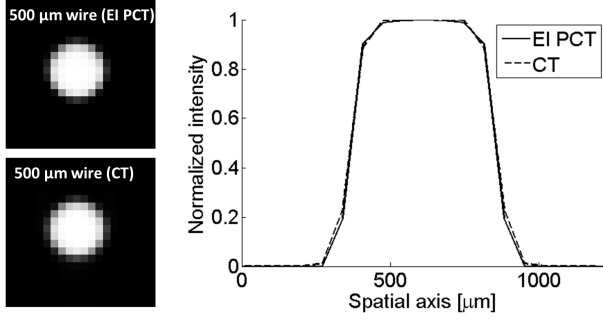


FIG. 3. Simulated EI PCT and CT images of a $500 \mu\text{m}$ diameter wire and horizontal plots across the respective images.

B. Extraction of the refraction angle image

In the following, the dependency on the rotation angle (θ) is dropped from the expressions for simplicity's sake. The propagation of noise from the raw EI PCT projections (I_L, I_R) into the extracted refraction angle image (α) can be estimated via the error propagation formula²⁰:

$$\begin{aligned} \sigma_\alpha^2 &= \left(\frac{\partial \alpha}{\partial I_L} \right)^2 \cdot \sigma_{I_L}^2 + \left(\frac{\partial \alpha}{\partial I_R} \right)^2 \cdot \sigma_{I_R}^2 \\ &= \left(\frac{\partial(F^{-1})}{\partial I_L} \right)^2 \cdot \sigma_{I_L}^2 + \left(\frac{\partial(F^{-1})}{\partial I_R} \right)^2 \cdot \sigma_{I_R}^2. \end{aligned} \quad (9)$$

Applying the chain rule and the rule of inverse functions and differentiation, this can be written as:

$$\sigma_\alpha^2 = \left(\frac{1}{I_R F'(\alpha)} \right)^2 \cdot \sigma_{I_L}^2 + \left(-\frac{I_L}{(I_R)^2 F'(\alpha)} \right)^2 \cdot \sigma_{I_R}^2. \quad (10)$$

Inserting:

$$F'(\alpha) = \frac{z_2}{M} \cdot \frac{C'(x_L + \frac{z_2 \alpha}{M}) C(x_R + \frac{z_2 \alpha}{M}) - C(x_L + \frac{z_2 \alpha}{M}) C'(x_R + \frac{z_2 \alpha}{M})}{(C(x_R + \frac{z_2 \alpha}{M}))^2}, \quad (11)$$

as well as $\sigma_{I_L}^2 = I_L$ and $\sigma_{I_R}^2 = I_R$, yields:

$$\sigma_\alpha^2 = \frac{K}{N}, \quad (12)$$

where K is a factor that depends on the refraction angle and the EI PCT setup:

$$K = \frac{2M^2}{(z_2)^2} \cdot \frac{C(x_L + \frac{z_2 \alpha}{M}) C(x_R + \frac{z_2 \alpha}{M})^2 + C(x_L + \frac{z_2 \alpha}{M})^2 C(x_R + \frac{z_2 \alpha}{M})}{(C'(x_L + \frac{z_2 \alpha}{M}) C(x_R + \frac{z_2 \alpha}{M}) - C(x_L + \frac{z_2 \alpha}{M}) C'(x_R + \frac{z_2 \alpha}{M}))^2}. \quad (13)$$

Note that for the special case of $\alpha = 0$, working points^{S237} 12 reduces to:
 $|x_L| = |x_R|$ and a symmetric illumination function, Eq.

$$\sigma_\alpha^2 = \frac{M^2}{N(z_2)^2} \cdot \frac{C(x_R)}{C'(x_R)^2}, \quad (14)$$

matching previously published results²¹.

According to Beer's law and Poisson statistics, in CT, the noise propagation from raw projections (I_{tr}) into attenuation images (A) is described by: $\sigma_A^2 = 1/N$. This allows expressing the variance of α in terms of the variance of A :

$$\sigma_\alpha^2 = K \cdot \sigma_A^2. \quad (15)$$

Due to the assumption of uncorrelated noise, both α and A have a constant NPS, and Eq. 15 implies the relation:

$$\text{NPS}_\alpha(\rho) = K \cdot \text{NPS}_A(\rho), \quad (16)$$

where ρ denotes the spatial frequency.

C. Recovery of the phase shift image

Considering that the integration operation (Eq. 6) required to recover the phase shift image from the refraction angle image correlates individual data points with each other, it is to be expected that the NPS of the phase shift image is not constant. Indeed, a one-dimensional discrete integration modulates the NPS at spatial frequency ρ by a factor $(\Delta x)^2/4 \cdot \sin^2(\pi\rho\Delta x)$ that depends on the multiplicative weight Δx . This is a combined effect of the integration itself, which corresponds to a multiplication with $1/(2\pi i\rho)$ in Fourier space, and the modulation transfer of the sampling process, which is given by $\pi\rho\Delta x/\sin(\pi\rho\Delta x)$. Multiplying and squaring both yields the above factor. Therefore, in the case of EI PCT, where the multiplicative weight is given by the sampling step ($\Delta x = d$), this yields:

$$\text{NPS}_\Phi(\rho) = \frac{d^2 k^2}{4 \cdot \sin^2(\pi\rho d)} \cdot \text{NPS}_\alpha(\rho). \quad (17)$$

The additional factor k^2 comes in because a multiplication by k is required to recover Φ from α . Equation 17 implies that NPS_Φ is shifted towards lower frequencies, and that it diverges for $\rho \rightarrow 0$. As discussed in Section IV, this ultimately affects the noise texture in the reconstructed phase tomograms.

Finally, by inserting Eq. 16 into Eq. 17, we can again express the NPS of Φ in terms of the NPS of A :

$$\text{NPS}_\Phi(\rho) = \frac{d^2 k^2}{4 \cdot \sin^2(\pi\rho d)} \cdot K \cdot \text{NPS}_A(\rho). \quad (18)$$

The variance of Φ can be calculated as $\sigma_\Phi^2 = \int \text{NPS}_\Phi(\rho) d\rho$.

D. Tomographic reconstruction

Having described the noise in the recovered phase shift image, we now analyze how the noise propagates into the phase tomograms. As was shown previously²⁸, the variance of tomograms reconstructed with the FBP can be

described by: $\sigma_\delta^2 = 2\pi \cdot \int_0^\infty \text{NPS}_{rad}(\rho) \rho d\rho$, assuming the sample is radially symmetric. NPS_{rad} is the radial NPS given by: $\text{NPS}_{rad}(\rho) = |\rho| \cdot |M_{alg}(\rho)|^2 \cdot \text{NPS}_{in}(\rho)$. Here, NPS_{in} refers to the NPS of the input data, and M_{alg} is the modulation transfer function of the FBP, which depends on the used filter function. With this formalism, the noise in the reconstructed phase tomograms (maps of δ) can be expressed as:

$$\sigma_\delta^2 = 2\pi \cdot \int_0^\infty \rho^2 \cdot |M_{alg}(\rho)|^2 \cdot \frac{d^2 k^2}{4 \cdot \sin^2(\pi\rho d)} \cdot K \cdot \text{NPS}_A(\rho) d\rho \quad (19)$$

$$\text{NPS}_{rad,\delta}(\rho) = |\rho| \cdot |M_{alg}(\rho)|^2 \cdot \frac{d^2 k^2}{4 \cdot \sin^2(\pi\rho d)} \cdot K \cdot \text{NPS}_A(\rho) \quad (20)$$

These equations are the first key result of this paper, as they enable characterizing the noise in EI PCT.

Analogously, the noise in attenuation tomograms (maps of β) reconstructed from CT data can be expressed as:

$$\sigma_\beta^2 = 2\pi \cdot \int_0^\infty \rho^2 \cdot |M_{alg}(\rho)|^2 \cdot \text{NPS}_A(\rho) d\rho \quad (21)$$

$$\text{NPS}_{rad,\beta}(\rho) = |\rho| \cdot |M_{alg}(\rho)|^2 \cdot \text{NPS}_A(\rho). \quad (22)$$

IV. ANALYSIS

A. Validity limits

Before using Eqs. 19 – 22 for a comparison of EI PCT and CT, we explore the validity limits of the error propagation formula (Eq. 9), which provided the basis for the above theory. For this purpose, theoretical predictions made via Eq. 15 were compared to results obtained from an EI PCT simulation code²⁹, for parameters matching an experimental setup installed in our labs at UCL. While a detailed description of the setup can be found elsewhere²¹, the relevant simulation parameters are summarized in Table I. The detector pixel size is assumed to match the detector mask period. Note that the working points correspond to the steepest points on the illumination function, as indicated by the derivative shown in Fig. 2(b).

Raw projections (I_L , I_R) were simulated for different refraction angles ($\alpha = -10, 0, 10 \mu\text{rad}$) covering a broad but realistic range when imaging biological samples. Each simulated signal contained 10^5 independent data points. Since the simulation code is based on an analytic model and does not replicate statistical fluctuations, uncorrelated Poisson noise was applied in a separate step for photon numbers in the range of $N = 10^1$

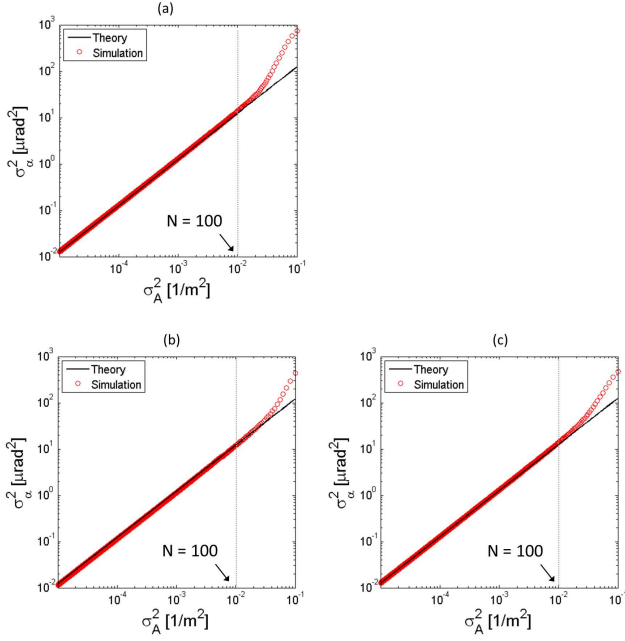


FIG. 4. The variance in the extracted refraction angle as a function of the variance in corresponding attenuation projections, as predicted by simulations and Eq. 15 for: (a) $\alpha = -10 \mu\text{rad}$, (b) $\alpha = 0 \mu\text{rad}$, (c) $\alpha = 10 \mu\text{rad}$.

-10^5 . Next, refraction angle images were extracted via Eq. 4, their variance calculated, and plotted against the variance in corresponding attenuation images (σ_A^2).

Fig. 4 shows the results obtained from the simulations, and those predicted by Eq. 15. As can be seen, both agree well up to a certain point, from which onward a deviation is apparent. This marks the validity limit of the error propagation formula (Eq. 9), which is applicable only when the noise transfer is linear. For low levels of noise, this assumption is met as the function F , which is used to extract α , can be approximated by a linear function (see Fig. 2(c)). However, this no longer holds for high noise levels; in that case, noise propagation follows the curvature of F , causing a disproportionate increase of the variance. Note that for the considered parameters, this occurs only for $N < 100$, a number that is exceeded

TABLE I. Parameters used for the EI PCT simulations

| | |
|--|---------------------|
| Source-to-sample distance (z_1): | 1.6 m |
| Sample-to-detector distance (z_2): | 0.4 m |
| Pre-sample mask period: | $68 \mu\text{m}$ |
| Pre-sample mask aperture: | $12 \mu\text{m}$ |
| Detector mask period: | $85 \mu\text{m}$ |
| Detector mask aperture: | $20 \mu\text{m}$ |
| X-ray energy: | 18 keV |
| Source focal spot (FWHM): | $70 \mu\text{m}$ |
| Left slope working point (x_L): | $-8.90 \mu\text{m}$ |
| Right slope working point (x_R): | $8.90 \mu\text{m}$ |

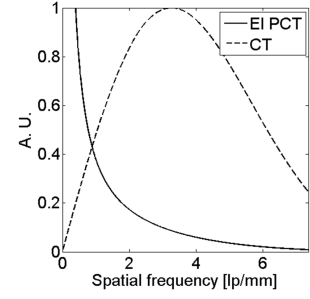


FIG. 5. Radial NPS in EI PCT and CT as predicted by Eqs. 20 and 22, displayed in arbitrary units.

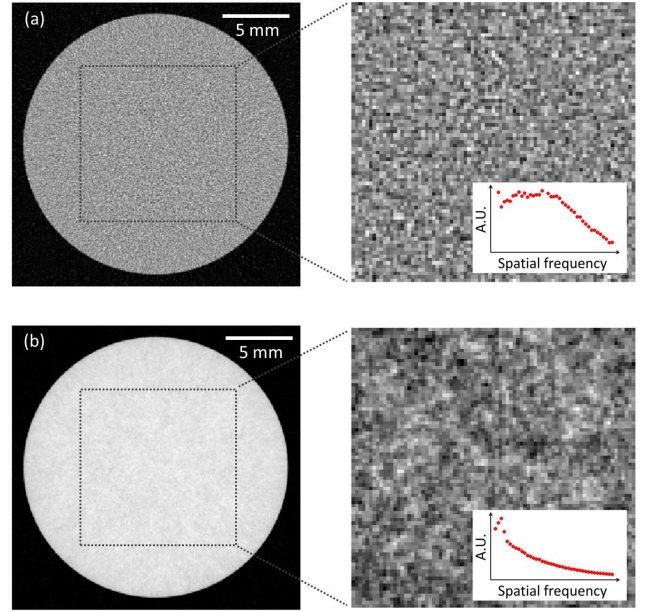


FIG. 6. Simulated tomograms of a PMMA cylinder of 2 cm diameter: (a) attenuation tomogram simulated for CT, (b) phase tomogram simulated for EI PCT.

in most practical situations.

B. Comparison of NPS

Equations 20 and 22 provide a description of the noise in EI PCT and CT across all spatial frequencies, allowing a comparison. The theoretical radial NPS curves for both modalities are shown in Fig. 5. These plots were created by evaluating Eqs. 20 and 22 for the parameters listed in Table I. In this example, the sampling step was assumed to match the pre-sample mask period ($d = 68 \mu\text{m}$). It was further assumed that $\text{NPS}_A = \text{constant}$ (a.u.) and $M_{alg} = |\text{sinc}^3(\rho d)|$, which is the modulation transfer function of the FBP with the Shepp-Logan fil-

ter and linear interpolation on a raster with spacing d during back projection³⁰. It is apparent that the radial NPS in phase tomograms is shifted towards the lower frequencies and, notably, diverges for $\rho \rightarrow 0$. As already noted above, this is due to the integration step required for the recovery of the phase shift image (Eq. 6), which is not necessary for the reconstruction of attenuation tomograms.

The effect of this shift is a fundamentally different noise texture in phase and attenuation tomograms, which has been observed previously for other PCT methods^{13,15,16}. To illustrate this point, phase tomograms of a PMMA cylinder (2 cm diameter) were simulated according to the routines and parameters described in Section IV A. Corresponding attenuation tomograms were simulated via Beer's law. The δ - and β -values of PMMA at the simulated energy (18 keV) were obtained from an online

database³¹. The sampling step in EI PCT, and hence the pixel size in CT (see Section III A), was assumed to be $d = 68 \mu\text{m}$. The number of photons was $N_0 = 10^3$, and the number of rotation angles was 1800, equally spaced over 180 degrees. The results are shown in Fig. 6; the contrast in the zoomed regions was adjusted to fully reveal the texture of the noise. As can be seen, the phase tomogram has a "blobbier" appearance, reflecting the higher proportion of low-frequency noise. NPS curves calculated from the central 80 x 80 pixels of the simulated images are shown as insets in the respective panels.

C. Comparison of CNR

Equations 19 and 21 enable the calculation of the CNR in phase and attenuation tomograms for any pair of adjacent materials (M_1, M_2), as well as their ratio:

$$\text{CNR}_\delta = \frac{k \cdot |\delta_{M_1} - \delta_{M_2}|}{\sigma_\delta} = \frac{k \cdot |\delta_{M_1} - \delta_{M_2}|}{\sqrt{2\pi \cdot \int_0^\infty |\rho|^2 \cdot |M_{alg}(\rho)|^2 \cdot \frac{d^2 k^2}{4 \sin^2(\pi \rho d)} \cdot K \cdot \text{NPS}_A(\rho) d\rho}} \quad (23)$$

$$\text{CNR}_\beta = \frac{2k \cdot |\beta_{M_1} - \beta_{M_2}|}{\sigma_\beta} = \frac{2k \cdot |\beta_{M_1} - \beta_{M_2}|}{\sqrt{2\pi \cdot \int_0^\infty |\rho|^2 \cdot |M_{alg}(\rho)|^2 \cdot \text{NPS}_A(\rho) d\rho}} \quad (24)$$

$$\frac{\text{CNR}_\delta}{\text{CNR}_\beta} = \frac{|\delta_{M_1} - \delta_{M_2}|}{|\beta_{M_1} - \beta_{M_2}|} \cdot \frac{1}{dk\sqrt{K}} \cdot \sqrt{\frac{\int_0^\infty |\rho|^2 \cdot |M_{alg}(\rho)|^2 d\rho}{\int_0^\infty \frac{|\rho|^2 \cdot |M_{alg}(\rho)|^2}{\sin^2(\pi \rho d)} d\rho}} \quad (25)$$

Equation 25 is the second key result of this article, as it allows a direct comparison of EI PCT and CT. It also shows that the relative performance of these modalities is very complex, and generally depends on the sample composition (via $\delta_{M_1}, \delta_{M_2}, \beta_{M_1}$ and β_{M_2}), the parameters of the EI PCT setup (via K), the x-ray energy (via the wave number k), the filter function of the FBP (via $|M_{alg}|$) and, finally, on the spatial resolution (via the sampling step d). Note that $\delta_{M_1}, \delta_{M_2}, \beta_{M_1}, \beta_{M_2}$ and K also implicitly depend on the wave number k . As tomographic reconstruction via FBP with the Shepp-Logan filter was assumed, Eq. 25 can be somewhat simplified; as was shown previously¹⁵, in this case the expression under the square root takes on the value of 3/8.

When fixing the parameters in Table I, Eq. 25 becomes a function of the sampling step (d), allowing analyzing the relative CNR as a function of spatial resolution. It can be seen that the relative CNR drops reciprocally with increasing sampling step; therefore, the coarser the spatial resolution, the lower the relative CNR. To evaluate the relative performance of EI PCT and CT, the so-called break-even point ($\text{CNR}_\delta = \text{CNR}_\beta$) must be considered,

which is reached when:

$$d = \frac{|\delta_{M_1} - \delta_{M_2}|}{|\beta_{M_1} - \beta_{M_2}|} \cdot \frac{1}{k\sqrt{K}} \cdot \sqrt{\frac{3}{8}} \quad (26)$$

The break-even point is generally sample dependent. To illustrate this, Eq. 25 was evaluated for three material combinations: PMMA/air, water/air and PMMA/water. These have been chosen as they approximate commonly encountered interfaces in biological tissues: PMMA is often considered a tissue-equivalent material and water and air are naturally present in biological systems. In all cases, it was assumed that the sample is radially symmetric, made of the first material, and embedded in the second. Again, the δ - and β -values of PMMA, air and water at the simulated energy (18 keV) were obtained from an online database³¹. The results are shown in Fig. 7. In all three panels, the arrow points to the break-even point, i.e. where EI PCT and CT perform equally well and below/above which the performance of EI PCT is superior/inferior to that of CT. As can be seen, the CNR ratio shows a strong dependence on the sampling

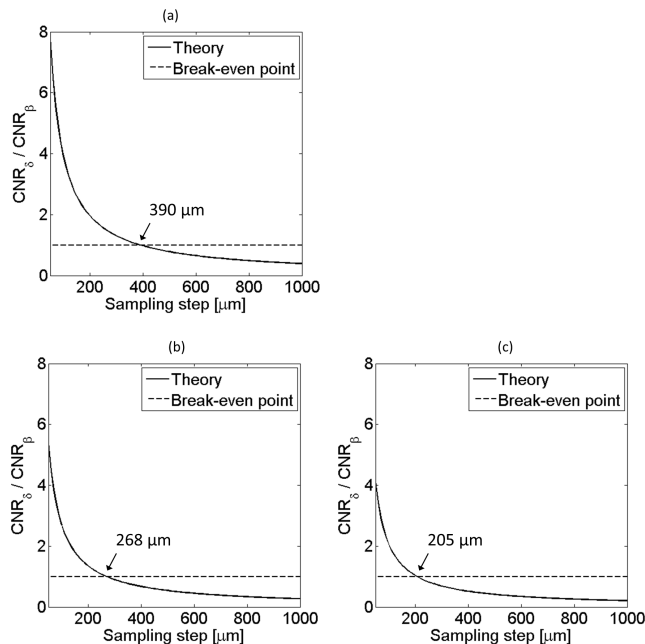


FIG. 7. Relative CNR of EI PCT and CT as a function of the sampling step (d) for three different material interfaces: (a) PMMA/air, (b) water/air, (c) PMMA/water.

step (i.e. the spatial resolution), with a general decrease for larger ones. Moreover, the dependence on the material combination can be observed, most apparently via the different break-even points, reached for $d = 390 \mu\text{m}$, $268 \mu\text{m}$ and $205 \mu\text{m}$ in the three cases. In addition to the theoretical curves for $\text{CNR}_\delta/\text{CNR}_\beta$, each panel in Fig. 7 contains numerical results, which were obtained by simulating phase tomograms via the routine described in Section IV A and by assuming the parameters listed in Table I. The number of photons was $N_0 = 10^3$. Corresponding attenuation tomograms were again simulated using Beer's law.

The above results were obtained for a specific set of parameters which was kept fixed; more generally, the best performance of EI PCT over CT can be obtained when these parameters are optimized for the specific imaging task. For example, Eq. 25 shows that a decrease of the setup-specific factor K also increases the CNR ratio, similarly to the sampling step. A theoretical analysis of how K is affected by system parameters such as the source and mask characteristics has been presented in previous work^{21,32}. For example, it has been shown that K scales with the steepness of the illumination function, and that a steeper illumination function can be obtained for smaller source focal spots or smaller apertures in the pre-sample mask.

V. SUMMARY AND DISCUSSION

A description of the noise (through NPS and variance) in EI PCT was provided and related to that in conventional, attenuation-based CT. Importantly, this revealed that the NPS in phase tomograms is characterized by a shift towards the lower spatial frequencies, as well as a divergence for $\rho \rightarrow 0$. This is a result of the integration step involved in the reconstruction process (recovery of the phase shift image), which is not needed for the reconstruction of attenuation tomograms. Consequently, phase tomograms contain a higher proportion of low frequency noise, which explains their slightly “blobby” appearance. The presented theory further allowed relating the CNR in phase tomograms to that in corresponding attenuation tomograms, enabling a direct comparison of EI PCT and CT. It was found that the relative performance of the two modalities depends in a complex way on the imaging setups, the reconstruction algorithm and the sample itself. Evaluating the relative CNR as a function of the spatial resolution has revealed that EI PCT has a superior performance for higher spatial resolutions (tens to hundreds of μm), and an inferior one for lower spatial resolutions (hundreds of μm to mm). These results follow the same trend that was observed previously for Talbot/Lau interferometry¹⁵. Note though that, for any spatial resolution, the CNR in EI PCT can be optimized through setup modifications that lead to a reduction of the factor K (see Eqs. 12 and 25).

In previous studies, the link between CNR and spatial resolution in PCT had been considered a drawback regarding its potential use for the clinical imaging of human patients³³. In such applications, spatial resolutions are typically bound to exceed hundreds of μm or even mm, in order to limit the delivered radiation dose and access large fields of view. While agreeing on this aspect, we would however like to emphasize the positive implications of this link on small animal and/or specimen imaging. In these areas, spatial resolutions of tens to hundreds of μm are often necessary to resolve features of interest, and are already encountered in conventional (attenuation-based) micro-CT scanners. In these applications, such high spatial resolutions can be achieved, since the associated increase in radiation dose is a lesser concern, and fields of view are typically smaller. Therefore, phase contrast micro-CT, if used as an alternative or addition to conventional micro-CT, could provide a real benefit, with substantial CNR improvements potentially achievable. In this context, note that spatial resolutions of tens of μm down to a few μm have been demonstrated to be feasible with EI, even when implemented in standard laboratories^{23,34}.

Finally, we would like to draw attention to the limitations of the presented analysis. First, it is based on assumptions (Section III A) that may not always be met in realistic imaging scenarios. For example, uncorrelated Poisson noise was assumed to be the only source of error in raw projections, while in practice contributions from

pixel cross-talk, vibrations or mask defects/misalignment could be present. Moreover, the theory was derived for a monochromatic x-ray beam, and it was assumed that EI PCT and CT are operated at the same energy. In practice, scans are typically performed with polychromatic beams and different spectra. These factors will have to be thoroughly studied in order to fully understand their effect on the relative performance of EI PCT and CT.

ACKNOWLEDGMENTS

This work was supported by the UK Engineering and Physical Sciences Research Council (Grant Nos. EP/L001381/1 and EP/I021884/1). PCD is supported by Marie Curie Career Integration Grant Nos. PCIG12-GA-2012-333990 within the Seventh Framework Programme of the European Union. The authors thank Dr Rainer Raupach for valuable comments and discussions.

The authors have no relevant conflicts of interest to disclose.

- ¹A. Bravin, P. Coan, and P. Suortti, "X-ray phase contrast imaging: from pre-clinical applications towards clinics," *Phys. Med. Biol.* **58**, R1–R35 (2013).
- ²A. Snigirev, I. Snigireva, V. Krohn, S. Kuznetsov, and I. Shelokov, "On the possibilities of x-ray phase contrast microimaging by coherent high energy synchrotron radiation," *Rev. Sci. Instrum.* **66**, 5486–5492 (1995).
- ³P. Cloetens, R. Barrett, J. Baruchel, J. Guigay, and M. Schlenker, "Phase objects in synchrotron radiation hard x-ray imaging," *J. Phys. D: Appl. Phys.* **29**, 133–146 (1996).
- ⁴S. Wilkins, T. Gureyev, D. Gao, A. Pogany, and A. Stevenson, "Phase-contrast imaging using polychromatic hard x-rays," *Nature* **384**, 335–338 (1996).
- ⁵C. David, B. Nohammer, H. Solak, and E. Ziegler, "Differential x-ray phase contrast imaging using a shearing interferometer," *Appl. Phys. Lett.* **81**, 3287–3289 (2002).
- ⁶A. Momose, S. Kawamoto, I. Koyama, Y. Hamaiishi, K. Takai, and Y. Suzuki, "Demonstration of x-ray Talbot interferometry," *Jap. J. Appl. Phys.* **42**, L866–L868 (2003).
- ⁷F. Pfeiffer, T. Weitkamp, O. Bunk, and C. David, "Phase retrieval and differential phase-contrast imaging with low-brilliance x-ray sources," *Nat. Phys.* **2**, 258–261 (2006).
- ⁸T. Davis, D. Gao, T. Gureyev, A. Stevenson, and S. Wilkins, "Phase-contrast imaging of weakly absorbing materials using hard x-rays," *Nature* **378**, 595–598 (1995).
- ⁹V. Ingal and E. Beliaevskaya, "X-ray plane-wave topography observation of the phase contrast from a non-crystalline object," *J. Phys. D: Appl. Phys.* **28**, 2314–2317 (1995).
- ¹⁰D. Chapman, W. Thomlinson, R. Johnston, D. Washburn, E. Pisano, N. Gmur, Z. Zhong, R. Menk, F. Arfelli, and D. Sayers, "Diffraction enhanced imaging," *Phys. Med. Biol.* **42**, 2015–2015 (1997).
- ¹¹A. Olivo, F. Arfelli, G. Cantatore, R. Longo, R. Menk, S. Pani, M. Prest, P. Poropat, L. Rigon, G. Tromba, E. Valazza, and E. Castelli, "An innovative digital imaging setup allowing a low-dose approach to phase contrast applications in the medical field," *Med. Phys.* **28**, 1610–1619 (2001).
- ¹²A. Olivo and R. Speller, "A coded-aperture technique allowing x-ray phase contrast imaging with conventional sources," *Appl. Phys. Lett.* **91**, 074106 (2007).
- ¹³C. Chou and M. Anastasio, "Noise texture and signal detectability in propagation-based x-ray phase-contrast tomography," *Med. Phys.* **37**, 270–281 (2010).
- ¹⁴T. Koehler, K. Engel, and E. Roessl, "Noise properties of grating-based x-ray phase contrast computed tomography," *Med. Phys.* **38**, 106–116 (2011).
- ¹⁵R. Raupach and T. Flohr, "Analytical evaluation of the signal and noise propagation in x-ray differential phase-contrast computed tomography," *Med. Phys.* **56**, 2219–2244 (2011).
- ¹⁶X. Tang, Y. Yang, and S. Tang, "Characterization of imaging performance in differential phase contrast CT compared with the conventional CT - noise power spectrum NPS(k)," *Med. Phys.* **38**, 4386–4395 (2011).
- ¹⁷T. Weber, P. Bartl, F. Bayer, J. Durst, W. Haas, T. Michel, A. Ritter, and G. Anton, "Noise in x-ray grating-based phase-contrast imaging," *Med. Phys.* **38**, 4133–4140 (2011).
- ¹⁸K. Li, N. Bevens, J. Zambelli, and G. Chen, "Fundamental relationship between the noise properties of grating-based differential phase contrast CT and absorption CT: theoretical framework using a cascaded system model and experimental validation," *Med. Phys.* **40**, 021908 (2013).
- ¹⁹Y. Nesterets and T. Gureyev, "Noise propagation in x-ray phase-contrast imaging and computed tomography," *J. Phys. D: Appl. Phys.* **47**, 105402 (2014).
- ²⁰P. Bevington and D. Robinson, "Data reduction and error analysis for the physical sciences," New York: McGraw-Hill, 58–64 (1969).
- ²¹P. Diemoz, C. Hagen, M. Endrizzi, and A. Olivo, "Sensitivity of laboratory based implementations of edge illumination x-ray phase contrast imaging," *Appl. Phys. Lett.* **103**, 244104 (2013).
- ²²P. Munro, C. Hagen, M. Szafraniec, and A. Olivo, "A simplified approach to quantitative x-ray phase imaging," *Opt. Express* **21**, 11187–11201 (2013).
- ²³P. Diemoz, F. Vittoria, and A. Olivo, "Spatial resolution of edge illumination x-ray phase contrast imaging," *Opt. Express* **22**, 15514–15529 (2014).
- ²⁴C. Hagen, P. Coan, A. Bravin, A. Olivo, and P. Diemoz, "A continuous sampling scheme for edge illumination x-ray phase contrast imaging," *J. Appl. Phys.* **118**, 054901 (2015).
- ²⁵C. Hagen, P. Munro, M. Endrizzi, P. Diemoz, and A. Olivo, "Low-dose phase contrast tomography with conventional x-ray sources," *Med. Phys.* **41**, 070701 (2014).
- ²⁶F. Noo and R. Clackdoyle and J. Pack, "A two-step Hilbert transform method for 2D image reconstruction," *Phys. Med. Biol.* **49**, 3903–3923 (2004).
- ²⁷P. Diemoz and A. Olivo, "On the origin of phase contrast in edge illumination x-ray phase-contrast imaging," *Opt. Express* **22**, 28199–28214 (2014).
- ²⁸H. Barrett and W. Swindell, "Radiological imaging - the theory of image formation, detection and processing," New York: Academic (1996).
- ²⁹F. Vittoria, P. Diemoz, M. Endrizzi, L. Rigon, F. Lopez, D. Dreossi, P. Munro, and A. Olivo, "Strategies for fast and efficient wave optics simulation of coded-aperture and other x-ray phase contrast imaging methods," *Appl. Opt.* **52**, 6940–6947 (2013).
- ³⁰A. Oppelt, "Imaging Systems for Medical Diagnostics," Publicis Erlangen (2005).
- ³¹B. Henke, E. Gullikson, and J. Davis, "X-ray interactions: photoabsorption, scattering, transmission and reflection at $E = 50$ –30000 eV, $Z = 1$ –92," *At. Data. Nucl. Data Tables* **54**, 181–342 (1993).
- ³²P. Diemoz, M. Endrizzi, C. Hagen, C. Rau, A. Bravin, R. Speller, I. Robinson, and A. Olivo, "Edge illumination x-ray phase contrast imaging: nanoradian sensitivity at synchrotrons and translation to conventional sources," *P. Phys. Conf. Series* **499**, 012006 (2014).
- ³³R. Raupach and T. Flohr, "Performance evaluation of x-ray differential phase-contrast computed tomography (PCT) with respect to medical imaging," *Med. Phys.* **39**, 4761–4774 (2012).
- ³⁴M. Endrizzi, F. Vittoria, P. Diemoz, R. Lorenzo, R. Speller, U. Wagner, C. Rau, I. Robinson, and A. Olivo, "Phase-contrast microscopy at high x-ray energy with a laboratory setup," *Opt. Letters* **39**, 3332–3335 (2014).